

Contents lists available at ScienceDirect

# Intermetallics

journal homepage: www.elsevier.com/locate/intermet





# Effect of hydrogen on thermal deformation behavior and microstructure evolution of MoNbHfZrTi refractory high-entropy alloy

Xiangyang Shen <sup>a</sup>, Feng Liu <sup>a</sup>, Jinyuan Guan <sup>a</sup>, Fuyu Dong <sup>a,\*</sup>, Yue Zhang <sup>a,\*\*</sup>, Zihe Guo <sup>a</sup>, Ye Yuan <sup>a</sup>, Binbin Wang <sup>b</sup>, Liangshun Luo <sup>b</sup>, Yanqing Su <sup>b</sup>, Jun Cheng <sup>c,\*\*\*</sup>, Xiaoguang Yuan <sup>a</sup>, Peter K. Liaw <sup>d</sup>

- <sup>a</sup> School of Materials Science and Engineering, Shenyang University of Technology, Shenyang, China
- <sup>b</sup> School of Materials Science and Engineering, Harbin Institute of Technology, Harbin, China
- <sup>c</sup> Northwest Institute for Nonferrous Metal Research, Shaanxi Key Laboratory of Biomedical Metal Materials, Xi'an, 710016, China
- d The Department of Materials Science and Engineering, University of Tennessee, Knoxville, TN, USA

#### ARTICLE INFO

#### Keywords: Liquid hydrogenation Refractory high-entropy alloy Stress Hardening

#### ABSTRACT

The study examined the thermal-deformation behavior of an MoNbHfZrTi refractory high-entropy alloy (RHEA), which were hydrogenated using a liquid hydrogenation method and then subjected to high-temperature uniaxial compression in the deformation temperature range of  $1100-1250~^{\circ}\text{C}$  and strain rate range of  $0.5-10^{-3}~\text{s}^{-1}$ . Test results showed that: (1) When the deformation temperature was between  $1100~\text{and}~1250~^{\circ}\text{C}$ , hydrogen addition led to increased high-temperature peak stress of the alloy at higher strain rates of  $0.5~\text{and}~10^{-1}~\text{s}^{-1}$ . At a low strain rate of  $\sim 10^{-2}~\text{s}^{-1}$ , the addition of hydrogen causes a decrease in the high-temperature peak stress. However, at a lower strain rate of  $\sim 10^{-3}~\text{s}^{-1}$ , hydrogen addition has insignificant effects on the high-temperature peak stress. (2) At a higher strain rate of  $\sim 0.5~\text{s}^{-1}$ , the major reasons for hydrogen-induced hardening of the peak stress were solution strengthening and dislocation pinning. (3) At a low strain rate of  $10^{-2}~\text{s}^{-1}$ , the reason for decrease of the peak stress was that the hydrogen addition promoted the formation of precipitated phases, thereby facilitating dynamic recrystallization (DRX), and making the microstructure more uniform at high temperatures.

#### 1. Introduction

In recent years, with the development of science and technology, the service environment of metal materials has become increasingly harsh, which has put forward higher requirements for the mechanical properties of materials. Thus, a large number of new metal materials have emerged one after another. In 2004, Yeh first proposed the concept of high-entropy alloys (HEAs), which are defined as containing five or more constituent elements, with the content of each element at between 5 and 35 at% [1–4]. The simple structure and excellent properties of HEAs are closely associated with their four major effects (high entropy [5], hysteretic diffusion [6], lattice distortion [7], and cocktail effects [8]). Therefore, they have received wide attention from a large number of scholars in the field of materials. The RHEA primarily comprises of

titanium, zirconium, hafnium, tungsten, niobium, molybdenum, tantalum, vanadium (Ti, Zr, Hf, W, Nb, Mo, Ta, and V, respectively), and other refractory elements [9]. Compared with traditional high-temperature alloys, RHEAs have higher high-temperature strength and thermal stability, and have broad application prospects in the field of aviation, aerospace, and nuclear reactors under complex working conditions [10–15]. However, due to coarse dendrite structure and casting defects, most cast RHEAs might only show limited mechanical properties [16]. In addition, the use of cold working is also limited due to the poor plasticity of RHEA at room temperature. Thermal-deformation processing at high temperatures can eliminate the coarse dendrite and columnar crystal structures in the cast metal and weld pores, microcracks, and other defects in the cast metal, so as to improve their density and mechanical properties [17–19]. However,

E-mail addresses: dongfuyu2002@163.com (F. Dong), yuezhang@sut.edu.cn (Y. Zhang), 524161386@qq.com (J. Cheng).

<sup>\*</sup> Corresponding author.

<sup>\*\*</sup> Corresponding author.

<sup>\*\*\*</sup> Corresponding author.

X. Shen et al. Intermetallics 166 (2024) 108193

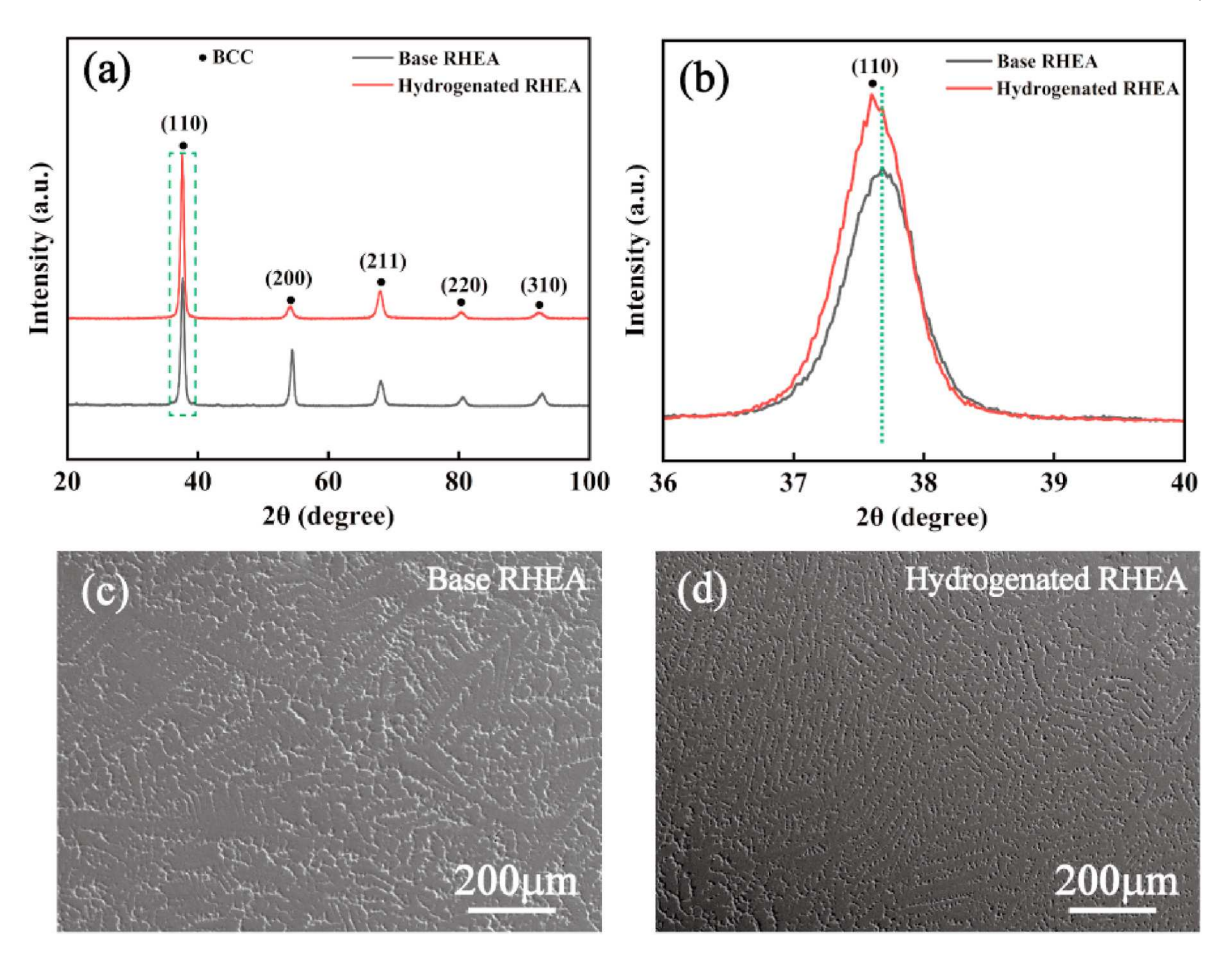


Fig. 1. (a) XRD patterns of base and hydrogenated MoNbHfZrTi RHEAs. (b) Enlarged image of (110) diffraction peaks in (a). (c, d) SEM images of base RHEA and hydrogenated RHEAs.

RHEAs still require extremely high deformation temperatures and great stresses during thermal deformation, thus making them difficult to process these alloys. At present, although a great deal of research has been conducted on the thermal-deformation behavior of HEAs, compared with traditional metal materials, HEAs still have much potential for development, particularly for RHEA.

As the smallest interstitial atom in the elemental periodic table, hydrogen is very likely to be introduced into a material during processing and production of metal materials, thus influencing their structures and properties. As early as the 19th century, Johnson has demonstrated that hydrogen-embrittlement failure could pose a serious threat to the safety and stability of metal components [20]. Compared with research on the hydrogen embrittlement of traditional metal materials, such as iron and steel materials, the research on hydrogen embrittlement of HEAs is only in its initial stage. At present, the main research systems have focused on the FCC structures of CoCrFeMnNi [21], CoCrFeNi [22], FeMnNiCrCo [23], TiZrHfMoNb [24], BCC structure of FeCuCrMnMo [25], CoCrNi [26], and FeCrCoNi [27]. Compared with conventional metal materials, hydrogen produces less plastic damage to HEAs under the same hydrogen charging conditions [28]. To date, hydrogen in the BCC RHEA is still rarely reported, in particular, the effects of hydrogen on RHEAs at high temperatures have been hardly studied. However, at high temperatures, the presence of hydrogen affects not only the high-temperature operation performance of metal materials, but also their hot working performance. Therefore, studying the effects of hydrogen on HEAs at high temperatures would be of significance for the use and processing of this material.

Since 1959, when it was found for the first time that hydrogen can improve the thermal-deformation capacity of cast Ti alloys [29], people

have begun to improve the processing performance of alloys constantly using hydrogen. This process includes refining their microstructures and hvdrogen developing the thermal hydrogen-assisted processing technology with the help hydrogen-induced plasticity, hydrogen-induced phase transition, and reversible alloying of hydrogen. To date, there remains great interest in the use of this technology in metal materials, especially refractory metal materials [30,31]. Based on the previous research findings, our research team has proposed a liquid hydrogenation method characterized by a fast hydrogenation rate and uniform hydrogen distribution following hydrogenation. Subsequently, a systematic study has been conducted on the microstructures, structures, and thermal-deformation behavior of Ti alloys [32] and Ti-aluminum (Al) alloy [33] after liquid hydrogenation. The relevant results verified that liquid hydrogenation can significantly improve the thermal-processing performance of materials. For RHEAs, there is no relevant research on whether thermal hydrogenation can assist in high-temperature formation. The present research assisted in broadening the application of the thermal-hydrogen technology and grasping the hot-working characteristics of RHEAs.

In this study, the MoNbHfZrTi RHEA was first treated by the liquid hydrogenation method and then subjected to the high-temperature uniaxial compression at a deformation temperature ranging from 1100 to 1250  $^{\circ}\text{C}$  at a strain rate ranging from 0.5 to  $10^{-3}~\text{s}^{-1}$ , and finally its thermal-deformation behavior examined.

### 2. Experimental materials and methods

The MoNbHfZrTi (at%) RHEA ingots were prepared by non-self-consumption high-vacuum electric arc furnace. The raw materials

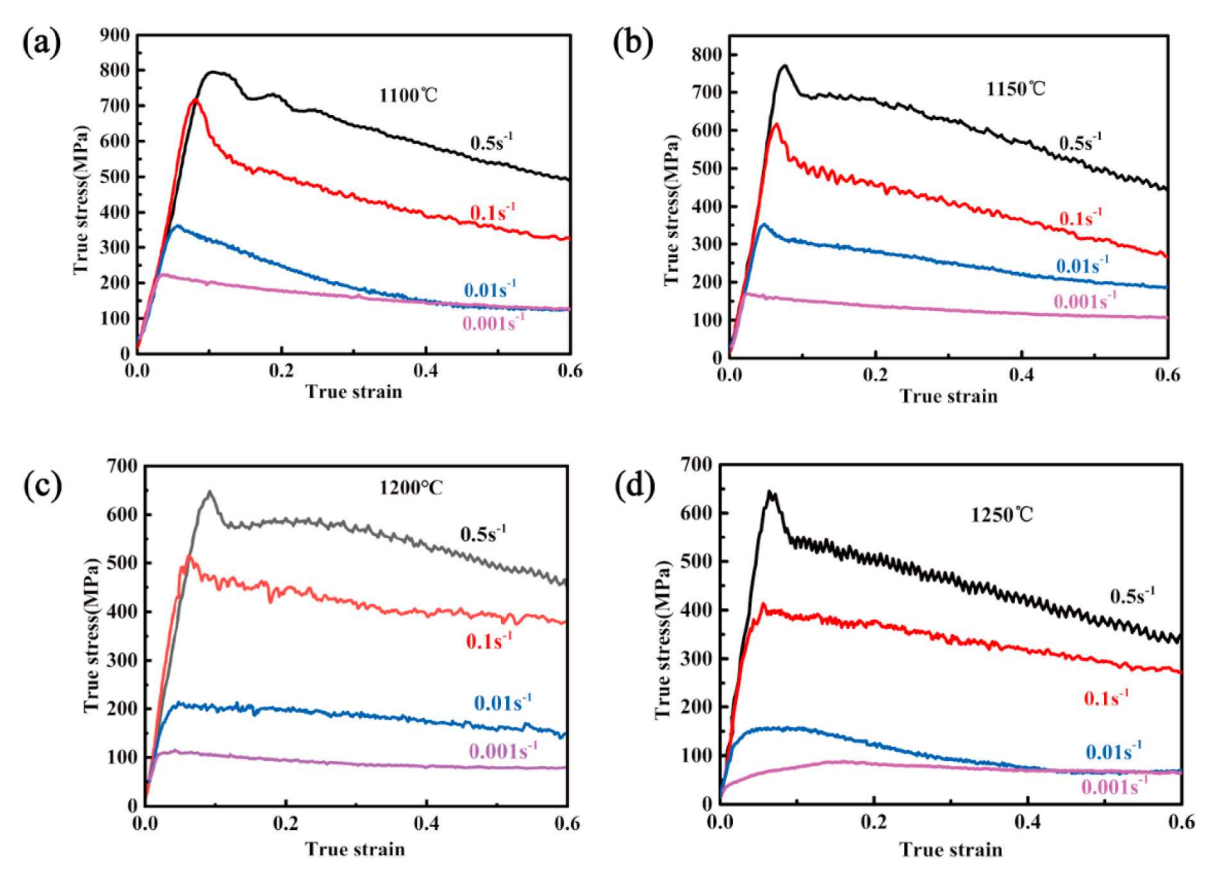


Fig. 2. True stress-strain curve of the hydrogenated MoNbHfZrTi RHEA. (a) 1100 °C, (b) 1150 °C, (c) 1200 °C, and (d) 1250 °C.

with purity higher than 99.9 wt% were provided by the Beijing Dream Material Technology Co., Ltd. High-purity argon (Ar) was used as the protective atmosphere during the melting process, and smelting repeated many times to ensure the uniformity of ingot compositions. The HEA ingots were subjected to hydrogenation with the liquid hydrogenation method, and the liquid hydrogenation of the alloy ingots completed after plasma arc remelting under a mixed atmosphere of 20 vol%  $\rm H_2 + 80$  vol% Ar.

Cylinders with dimensions of  $\Phi6~\text{mm}\times9~\text{mm}$  were cut from liquid hydrogenation button ingots by wire-electrode cutting for thermal compression experiments. The hydrogen content of all wire-electrode cutting samples was determined with a TCH-600 oxygen and nitrogen hydrogen analyzer (Leco Corp., St. Joseph, MI, USA), and the actual hydrogen content is 230 ppm. A high-temperature compression test was conducted with the Gleeble 3500 thermal simulation testing machine (Dynamic Systems, Inc., Poenstenkill, NY, USA), at deformation temperatures of 1100, 1150, 1200, and 1250 °C, strain rates of 0.5, 0.1,  $10^{-2}$ , and  $10^{-3}$  s<sup>-1</sup>, and deformation at 60 %. The specimen was heated to the deformation temperature at a heating rate of 10  $^{\circ}\text{C/s},$  temperature maintained for 180 s, and the specimen subjected to compressive deformation at a preset strain rate. The equipment cavity was prevacuumed to 2 Pa, using a vacuum pump and then filled with highpurity Ar to prevent high-temperature oxidation of the specimen prior to heating. Water quenching was performed to preserve the hightemperature deformed structure upon specimen compression. A scanning electron microscope (SEM, S-3400 N), transmission electron microscope (TEM, JEM-2100), and electron backscatter diffraction (EBSD) were used to analyze the microstructures and structures of the initial material and deformed specimens. To observe high-temperature microstructure following hot compression, perpendicular cuts were made along the center direction of the compressed specimen. The cut surface parallel to the compression direction was mechanically polished until the absence of any scratches. Then, electrolytic polishing was

performed to obtain a mirror-like surface. The electrolytic polishing solution consisted of 6 vol% HClO4, 35 vol%  $C_4H_{10}O$ , and 59 vol%  $CH_4O$ . Liquid nitrogen was used as the cooling medium during electrolytic polishing, and the current kept at 2.5 A. EBSD was used to observe the microstructure of hydrogenated thermally-compressed samples. A Channel 5 software was used to process all EBSD data to obtain inverse pole figure (IPF) plots, grain-boundary (GB) plots, and local misorientation (LM) plots. In the TEM analysis, the sample was first ground to a thickness of less than 50  $\mu$ m, and then the sample was ion thinned, using the Gatan 691. An XRD-7000 X-ray diffractometer (Shimadzu Corp., Kyoto, Japan) was employed for phase identification, with a scanning range of 20–100° and a scanning speed of 5°/min.

### 3. Results

# 3.1. Initial microstructure

The examination of XRD patterns of base and hydrogenated MoNbHfZrTi RHEAs is shown in Fig. 1(a). All samples exhibited a single BCC structure. As presented in Fig. 1(b), the (110) diffraction peak of the hydrogenated alloy tends to move towards a lower angle, compared with the base alloy, which indicates that the hydrogen atoms exist as interstitials in the BCC crystalline lattice. An SEM images of the microstructure of base and hydrogenated RHEAs showed a typical dendrite structure, as exhibited in Fig. 1(c) and (d).

# 3.2. High-temperature stress-strain behaviors

The true stress-true strain curve of hydrogenated RHEA was determined at different temperatures (1100–1250  $^{\circ}$ C) and strain rates (0.5–10 $^{-3}$  s $^{-1}$ ). The curve showed that under all thermal-compression conditions, the stress increased sharply to the peak stress with increasing strain and then decreased or reached a steady state (Fig. 2(a)–

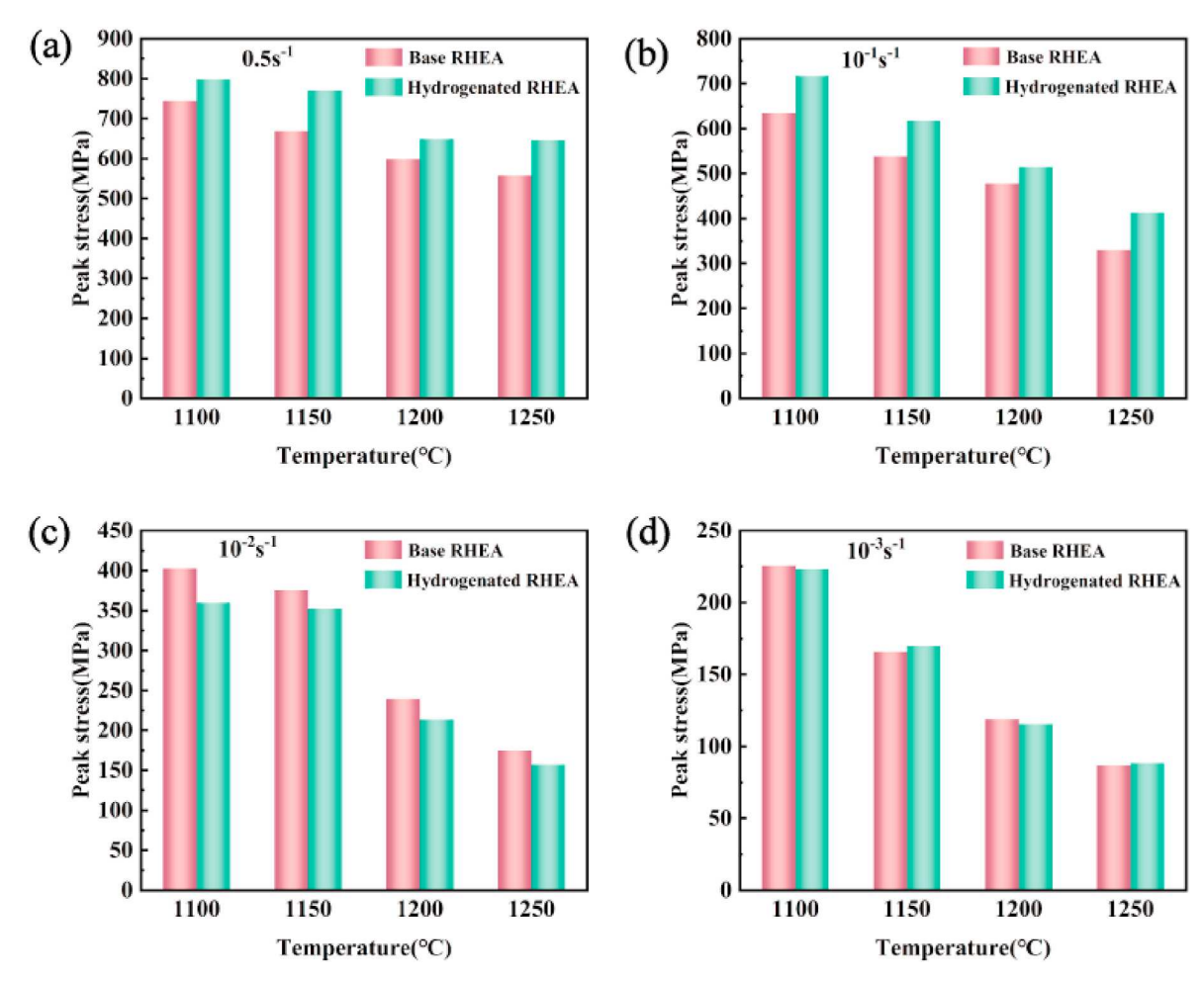


Fig. 3. Comparison of peak stresses of base and hydrogenated MoNbHfZrTi RHEAs under different hot deformation conditions. (a) 0.5, (b)  $10^{-1}$ , (c)  $10^{-2}$ , and (d)  $10^{-3}$  e<sup>-1</sup>

(d)). Early transient increase in the stress has been associated with the dislocation generation and proliferation, while continuous softening of the stress after the peak stress associated with DRX [34–38]. At high strain rates of  $\sim\!0.5~\text{s}^{-1}$ , a sudden drop in the stress after the peak stress has been observed in all stress-strain curves, which is associated with the unlocking of Cottrell atmosphere or chemical short-range ordered (SRO) pinning dislocations (Fig. 2(c)) [39]. At a high temperature of  $\sim\!1200~\text{C}$  and a low strain rate of  $\sim\!10^{-3}~\text{s}^{-1}$ , the flow stress after the peak stress was more likely to flow stably due to the dynamic equilibrium between the work hardening and dynamic recovery. The peak stress at different temperatures and strain rates showed that the peak stress decreased with increasing the temperature and decreasing the strain rate.

It is worth noting that the serration were observed on the stressstrain curve. With the increase of temperature, the serrated characteristics in the stress-strain curve became obvious at a strain rate of  $\sim 0.5$ s<sup>-1</sup>. The occurrence of this serrated plastic flow can be attributed to dynamic strain aging (DSA) [40]. DSA is a process of simultaneous deformation and aging, which is usually caused by the interaction between solute atoms and mobile dislocations [41,42]. It is well known that the solute atoms in the alloy have a pinning effect on the dislocation, and the dislocation will break away from this hindrance. This repeated locking and unlocking process led to the serrated characteristics in the stress-strain curve [43]. With the increase of temperature, the diffusion rate of solute atoms was accelerated, resulting in the rapid formation of solute atmospheres near the dislocation, and the dislocation can be quickly separated from the atmospheres. In other words, the number of repeated action of solute atoms increased, which led to a significant increase in the number of serrations in the stress-strain curve

at 1250 °C/0.5 s<sup>-1</sup>.

In the early stage, we have studied the hot-deformation behavior of the base MoNbHfZrTi in detail, and obtained the stress peaks under different conditions [44]. Furthermore, the peak stresses of the base and hydrogenated RHEAs at different deformation temperatures and strain rates were plotted in Fig. 3. Based on a comparison of the magnitude of the peak stress before and after hydrogenation, a peak stress was found to be associated with the strain rate. Under a high strain rate (0.5 and  $10^{-1}~\rm s^{-1}$ ), a significant peak stress hardening occurred in hydrogenated alloys. At a lower strain rate of  $\sim 10^{-2}~\rm s^{-1}$ , peak-stress softening occurred in the hydrogenated alloys. However, compared with the base alloy, the peak stress of hydrogenated alloy changed little at a lower strain rate of  $\sim 10^{-3}~\rm s^{-1}$ .

# 3.3. High-temperature microstructure at high strain rates

To further analyze the reasons for hardening and softening of peak stresses at different strain rates, the high-temperature microstructure of the compressed sample cores was observed by SEM. An SEM image was examined concerning the high-temperature microstructure of the hydrogenated MoNbTaZrTi RHEA at a large strain rate of  $\sim\!0.5~\rm s^{-1}$  and different temperatures (1100–1250 °C) following hot compression (Fig. 4). After thermal compression, a typical "flow line " type feature gradually formed at the sample center. The original structure, grain boundaries, second phase, and segregation gradually formed a hotprocessed fiber structure. The fiber structure wrapped with the original grains is few and narrow (Fig. 4(a) and (b)). As the temperature increased, the fiber structure increased significantly. (Fig. 4(c) and (d)).

X. Shen et al. Intermetallics 166 (2024) 108193

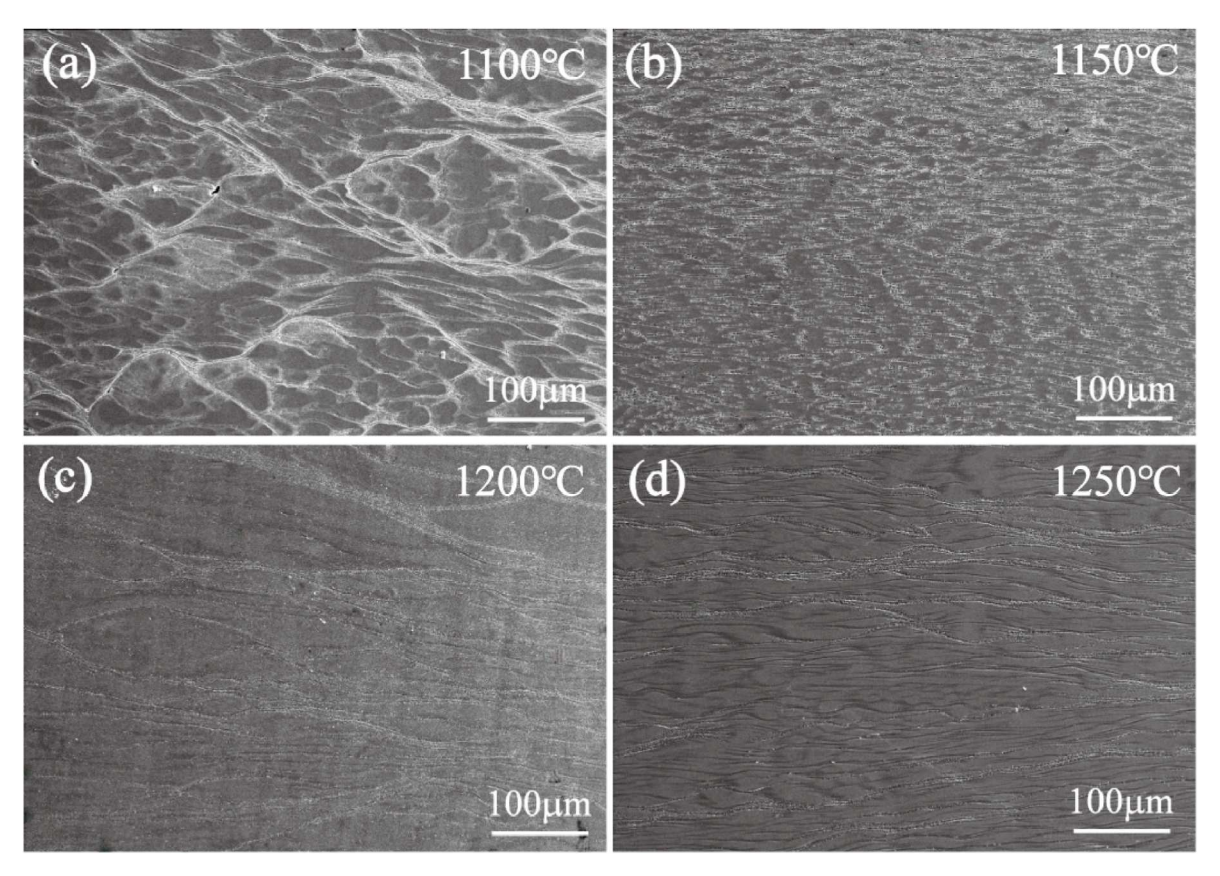


Fig. 4. SEM images of the hydrogenated RHEA at a strain rate of  $0.5~\text{s}^{-1}$  and different temperatures following hot deformation. (a) 1100~°C, (b) 1150~°C, (c) 1200~°C, and (d) 1250~°C.

At this point, the area of the original fragmented structure became smaller. Due to the short deformation time at a high strain rate of  $0.5 \, \mathrm{s}^{-1}$ , it was impossible to provide sufficient time for the movement of atomic diffusion and dislocation, such that the alloy could not be fully deformed. As a result, its rheological resistance was large.

# 3.4. Formation of precipitated phases at low strain rates

A SEM image of the high-temperature microstructure of the hydrogenated MoNbHfZrTi RHEA at different temperatures (1100, 1150, 1200, and 1250 °C) and low strain rate  $(10^{-2} \text{ and } 10^{-3} \text{ s}^{-1})$  following hot compression was examined (Fig. 5). Under high-power SEM, fine particles were observed to precipitate along the deformation fiber structure, being less than microns in size and small in number, dispersed (Fig. 5(a)). The number of precipitated phases gradually increased as the deformation temperature increased (Fig. 5(b)). Due to a further increase in the deformation temperature, the precipitated phases increased more significantly in the number and size and were concentrated at the deformation fiber structure (Fig. 5(c)). When the deformation temperature reached 1250 °C, the precipitated phase became thick and exhibited rod shapes (Fig. 5(d)). Under the strain rate of  $10^{-2}$  and  $10^{-3}$ s<sup>-1</sup>, the size and number of precipitated phases in the alloy show similar trends. Fine particles were precipitated along the deformation-fiber structure (Fig. 5(e)) and, as the deformation temperature increased, the precipitated phases increased significantly in the number and size (Fig. 5(f) and (g)). When the deformation temperature reached 1250  $^{\circ}$ C, larger precipitated phases were clearly observed (Fig. 5(h)). The microstructure after hot compression at 1250  $^{\circ}\text{C}/10^{-3}~\text{s}^{-1}$  was analyzed by SEM-EDS, as shown in Table 1. The results show that Hf is enriched in the dendrite region of the alloy, and the composition of the white precipitated phase is very similar to that of the dendrite region.

In the microstructures at higher strain rates above, no formation of

precipitated phases was observed. With increasing temperature and decreasing strain rate, the size of the precipitated phase increased, indicating that the growth of precipitated phases required certain energy conditions. The rise of temperature facilitated further growth of the precipitated phase, and decreasing strain rate provided sufficient time for the precipitated phase to form and grow. Subsequently, the precipitated phase generated along the boundaries of fragmented original grains reduced the obstruction of dislocation movement caused by the grain boundary, which in turn reduced the high-temperature deformation strength of the material. At a lower strain rate of  $10^{-3}~\rm s^{-1}$ , a more significant precipitation phase was observed, but the deformation resistance at this time was already very small,  $\sim \! 100~\rm MPa$ . Therefore, even if the precipitate caused softening, the peak stress change was limited.

Fig. 6(a) is the TEM image of the hydrogenated MoNbHfZrTi RHEA after hot compression at 1250  $^{\circ}\text{C}/10^{-3}~\text{s}^{-1}.$  The white rod-like or granular precipitated phase is distributed on the gray matrix of the alloy, which is consistent with the results observed by the SEM (Fig. 6(d)). The selected area electron diffraction (SAED) pattern in Fig. 6(b) can determine that the alloy matrix is a disordered BCC solid-solution structure. At the same time, the SAED pattern in Fig. 6(c) shows that the precipitated phase is also a BCC structure. The high temperature and low strain rate during hot deformation provide sufficient energy and time for the formation of precipitated phase, respectively.

# 3.5. DRX behavior of the hydrogenated MoNbHfZrTi RHEA

It is well known that the softening mechanism of the high-temperature deformation of materials is primarily associated with DRX, and this process is highly dependent on the microstructure of the material, such as the size and number of precipitated phases [45]. To this end, the effects of hydrogen precipitations on the DRX of the

X. Shen et al. Intermetallics 166 (2024) 108193

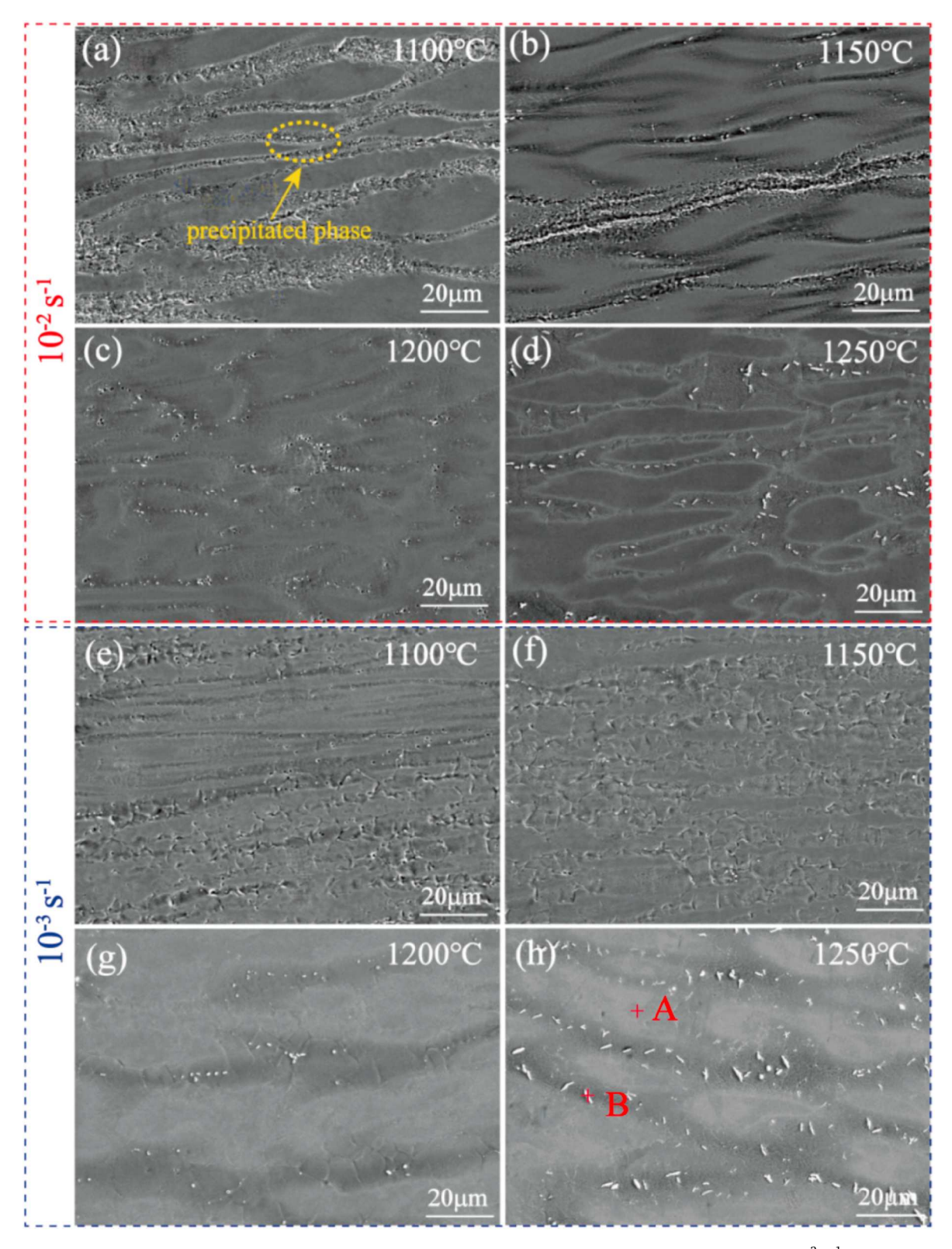


Fig. 5. SEM images of the hydrogenated RHEA at various temperatures and strain rates following hot deformation. (a)  $1100 \,^{\circ}\text{C}/10^{-2} \,^{-1}$ , (b)  $1150 \,^{\circ}\text{C}/10^{-2} \,^{-1}$ , (c)  $1200 \,^{\circ}\text{C}/10^{-2} \,^{-2} \,^{-1}$ , (d)  $1250 \,^{\circ}\text{C}/10^{-2} \,^{-2} \,^{-1}$ , (e)  $1100 \,^{\circ}\text{C}/10^{-3} \,^{-3} \,^{-1}$ , (f)  $1150 \,^{\circ}\text{C}/10^{-3} \,^{-3} \,^{-1}$ , (g)  $1200 \,^{\circ}\text{C}/10^{-3} \,^{-3} \,^{-1}$ , and (h)  $1250 \,^{\circ}\text{C}/10^{-3} \,^{-3} \,^{-1}$ .

MoNbHfZrTi RHEA following hydrogenation were examined. The EBSD observation was conducted of samples at a strain rate of  $10^{-2}~\rm s^{-1}$  and different deformation temperatures (1100 and 1250 °C, observation sites all located in the center area of uniform sample deformation) and a comparison performed with the DRX process of base alloys, as shown in Fig. 7.

The inverse pole figure (IPF), grain boundary (GB), and local misorientation maps (LM) of these alloys were determined under different deformation conditions. According to the key stereographic triangle, the color of the IPF diagram shows the crystallographic orientation parallel to the compression axis. In the GB diagram, red represents low-angle grain boundaries ( $2^{\circ} \leq \theta < 15^{\circ}$ , LAGBs), and blue

Table 1
Chemical compositions of the dendritic (A) and precipitated phase (B) in Fig. 5
(h) measured by the SEM-EDS (the atomic percentage).

Region	Zr	Nb	Mo	Ti	Hf
Dendrite (A) Precipitated phase (B)	13.51	20.26	15.39	18.02	32.82
	16.58	15.69	14.89	17.80	35.04

denotes high-angle grain boundaries ( $\theta \ge 15^{\circ}$ , HAGBs). Fig. 7 (a) and (d) are the IPF images of the base and hydrogenated RHEAs after hot compression at  $1100 \, {}^{\circ}\text{C}/10^{-2} \, \text{s}^{-1}$ , respectively. The necklace-like structure perpendicular to the compression direction showed fine, orthoscopic DRX grains regrown along the boundaries of the original fragmented recrystallized grains. These fine crystalline grains joined together to form a fiber strip during thermal deformation. Table 2 summarizes the recrystallization area fraction (fDRX), average recrystallized grain size ( $D_{\mathrm{DRX}}$ ), low-angle grain boundaries (LAGBs) and highangle grain boundaries (HAGBs) of base and hydrogenated RHEAs at a strain rate of 10<sup>-2</sup> s<sup>-1</sup> and different deformation temperatures. Under the same deformation conditions, the  $f_{DRX}$  of the hydrogenated alloy is 40.1 %, which is significantly higher than 23.4 % of the base alloy. This trend indicates that the addition of hydrogen promotes the occurrence of DRX. The phenomenon is further confirmed by the increase of highangle grain boundaries from 18.4 % to 32.2 % in the corresponding GB diagram (Fig. 7(b) and (e)). When the temperature rises to 1250 °C, the DRX degree and DDRX of the hydrogenated RHEA greatly increased

It is worth noting that the fine grains located inside the initial grains are observed in Fig. 7(g), and the transformation from LAGBs to HAGBs is also found in Fig. 7(h). These are typical characteristics of continuous dynamic recrystallization (CDRX). During the hot-deformation process, the misorientation of the sub-structures increases by continuously absorbing the surrounding dislocations until the CDRX grains with LAGBs are formed. For RHEAs, the CDRX mechanism generally occurs at high temperatures and low strain rates [46]. As shown in the LM pattern

of base and hydrogenated RHEA (Fig. 7(c), (f) and (i)), the DRX region was located around coarse grains with low local misorientation, while the local misorientation in the DRX region was very low. The average value of local misorientation was positively correlated with the average level of the dislocation density. In other words, a higher overall dislocation density resulted in a greater average value of local misorientation. At  $1100\,^{\circ}$ C/ $10^{-2}\,\text{s}^{-1}$ , as shown in Fig. 7(c) and (f), the average local misorientation of the hydrogenated RHEA is significantly lower than that of the base RHEA, which indicates that the enhanced DRX can reduce the dislocation density and the degree of work hardening. With increasing the temperature, the average local misorientation of the hydrogenated RHEA decreases significantly, as shown in Fig. 7(i).

#### 4. Discussion

### 4.1. Hydrogen-induced hardening at a high strain rate

The peak stress of the hydrogenated MoNbHfZrTi RHEA increased with hydrogen addition at high strain rates (0.5 and  $10^{-1}~\rm s^{-1}$ ). This is mainly attributed to the solid solution strengthening effect induced by hydrogen. It is well known that dislocation motion is a common mechanism for plastic deformation of alloys [47]. Plastic deformation in BCC alloys is dominated by screw dislocations [48]. However, RHEAs are different from other dilute alloys. It has been shown that the excellent elevated temperature strength of CrMoNbV and NbTaTiV RHEAs are mainly caused by edge dislocations [49]. Recently, Tseng et al. [50] found that the slip mode of HfMoNbTaW RHEA is screw dislocation at room temperature, while the slip mode changes to edge dislocation at high temperature plastic deformation of MoNbHfZrTi RHEA is mainly controlled by edge dislocations.

As an interstitials, hydrogen atoms easily accumulate in the compressive stress region of edge dislocation. Hence, hydrogen can enhance the pinning effect of edge dislocations and hinder its

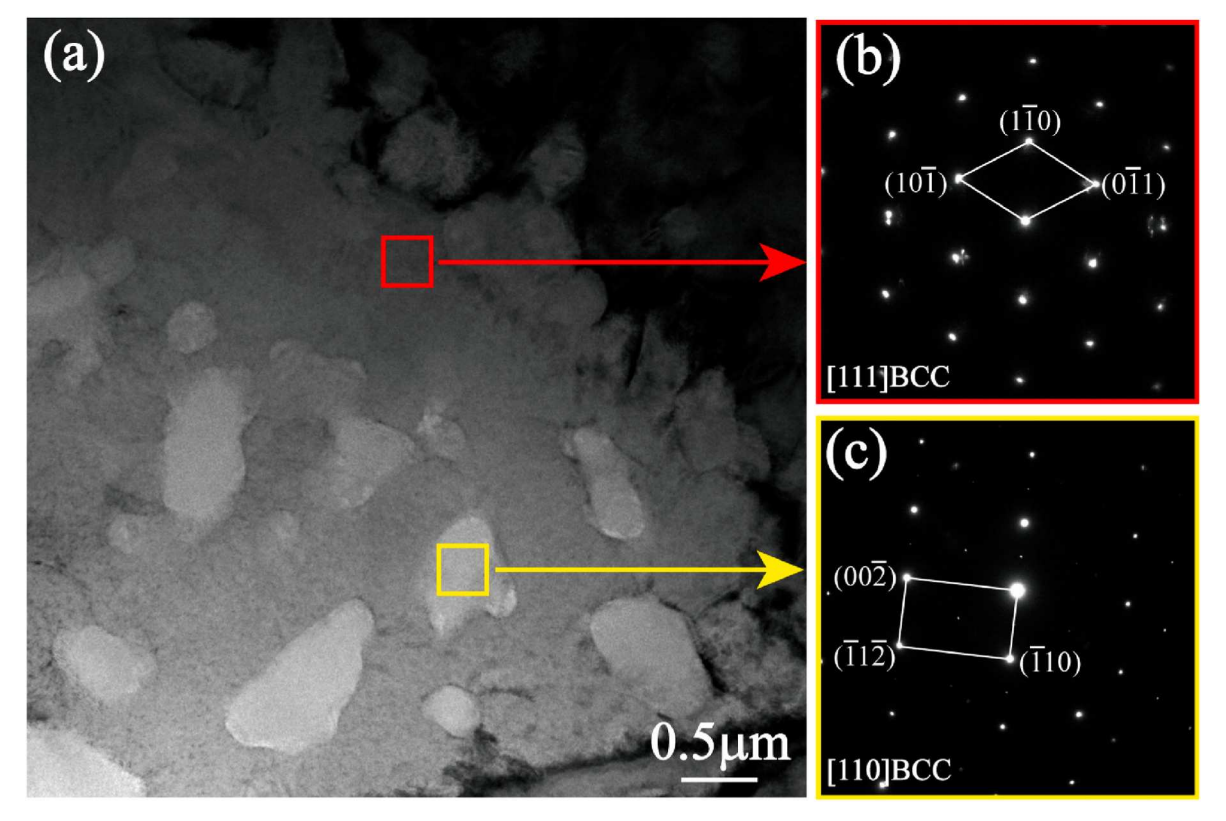


Fig. 6. (a) TEM image of the hydrogenated RHEA deformed at 1250 °C/10<sup>-3</sup> s<sup>-1</sup>. (b, c) The SAED patterns corresponding to the matrix and precipitated phases.

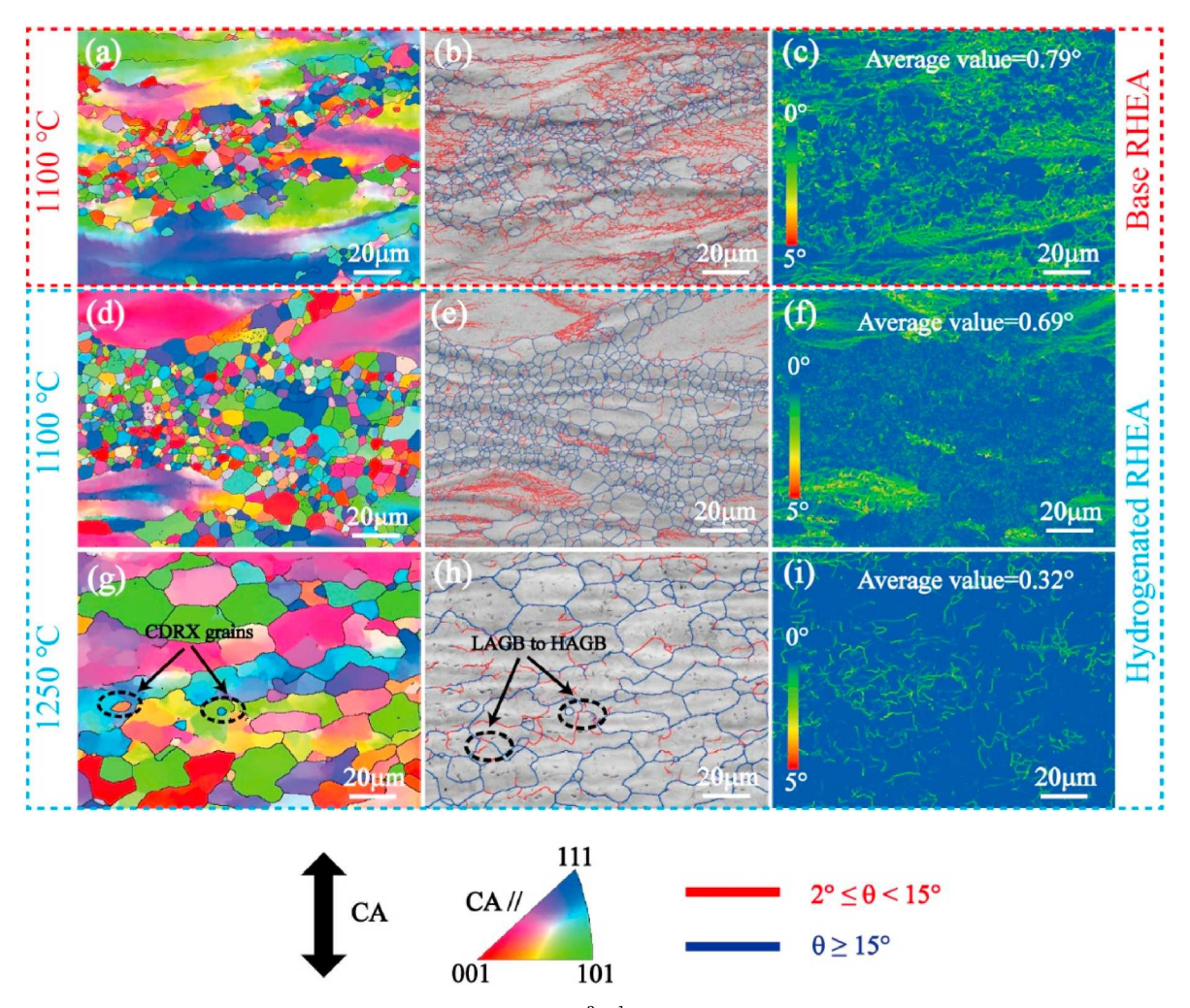


Fig. 7. EBSD patterns of the base and hydrogenated RHEAs at a strain rate of  $10^{-2}$  s<sup>-1</sup> and different temperatures. (a) IPF, (b) GB, and (c) LM maps of the base RHEA at 1100 °C; (d) IPF, (e) GB, and (f) LM maps of the hydrogenated RHEA at 1100 °C; (g) IPF, (h) GB, and (i) LM maps of the hydrogenated RHEA at 1250 °C.

**Table 2** The  $f_{DRX}$ ,  $D_{DRX}$ , LAGBs, and HAGBs of the base and hydrogenated RHEAs.

Alloys	Temperature (°C)	f <sub>DRX</sub> (%)	D <sub>DRX</sub> (μm)	LAGBs (%)	HAGBs (%)
Base RHEA	1100	23.4	4.8	81.6	18.4
Hydrogenated RHEA	1100 1250	40.1 73.2	5.4 21.7	67.8 25.1	32.2 74.9

movement, which leads to the strengthening of work hardening of alloy [51]. On the other hand, due to the high strain rate during thermal deformation, dislocations do not have enough time to annihilate and cancel. The strengthening effect between hydrogen and edge dislocations is higher than the softening effect of dynamic recovery. Therefore, at high strain rate, the peak stress of hydrogenated RHEA is higher than that of base RHEA.

### 4.2. Effects of hydrogen precipitation on DRX

Recrystallization is defined as "the formation of new grain structures following the formation and migration of high-angle grain boundaries driven by the stored energy in deformed materials" [52]. During thermal deformation, the DRX process is influenced by precipitated phase particles, which change the stored deformation energy and thus affect the driving force of recrystallization. In addition, these particles can significantly change the formation and migration of HAGBs [53]. They

are formed before, after, or concurrently with recrystallization, which also results in complex interactions with the recrystallization process. They can delay or accelerate recrystallization, depending on their size, number, and spatial distribution.

Due to their complexity, the effects of precipitated phase particles on recrystallization behavior were summarized below. On one hand, the effects of finely dispersed particles on recrystallization are generally explained by Zener pinning theory [54]. This theory points out that finely dispersed precipitated phases tend to hinder the movement of grain boundaries and further slow-down recrystallization and grain growth. On the other hand, the effects of coarse second-phase particles recrystallization are almost entirely concentrated particle-stimulated nucleation (PSN), which often leads to the accelerated DRX. Similar to most nucleation mechanisms, two necessary conditions need to be met for nucleation. One is the generation of HAGBs and the other the requirement of reaching the critical nucleation size [55]. The critical nucleation size of PSN cannot be calculated accurately as it is not a constant, but it is generally considered that PSN tends to occur at precipitated phase particles >1  $\mu m$ . Kondad et al. [56] have demonstrated that PSN occurs in precipitated phase particles of approximately 1.5–2 μm using the 3D-EBSD technology. In this section, in the hydrogenated MoNbHfZrTi RHEA, a 1–2 µm precipitated phase was produced in the microstructure. This feature meant that it satisfied the nucleation conditions of PSN and can accelerate DRX, resulting in stress softening [57–60].

#### 5. Conclusions

A high-temperature uniaxial compression experiment was carried out on the hydrogenated MoNbHfZrTi RHEA at different temperatures (1100–1250  $^{\circ}$ C) and different strain rates (0.5–10 $^{-3}$  s $^{-1}$ ). The effects of hydrogen on the elevated-temperature deformation behavior of HEAs under different heat deformation conditions were examined by SEM and EBSD methods. The following conclusions were drawn.

- (1) When thermal deformation occurred at a large strain rate (0.5 and  $10^{-1}$  s<sup>-1</sup>), the peak stress of the hydrogenated samples increased. At lower strain rates ( $\sim 10^{-2}$  s<sup>-1</sup>), the peak stress of the hydrogenated samples decreases and, at even lower strain rates ( $\sim 10^{-3}$  s<sup>-1</sup>), there were no significant changes due to the low peak stress.
- (2) At a large strain rate (0.5 and 10<sup>-1</sup> s<sup>-1</sup>), only a few thermal processing fiber structures were generated in the hydrogenated sample, which had a small size and many fragmented original structures. The peak stress of the hydrogenated samples was hardened during thermal deformation as a result of the pinning effect and solution-strengthening effects of hydrogen.
- (3) At a low strain rate ( $\sim 10^{-2} \ s^{-1}$ ), the thermal-processing fiber structure in the samples became more "slender," suggesting sufficient deformation. The addition of hydrogen facilitated the generation of precipitated phases in HEAs at smaller strain rates. The DRX accelerated in the precipitated phase particle formation satisfying the conditions of the PSN mechanism, thereby decreasing the hydrogen-induced peak stress of these alloys.

#### CRediT authorship contribution statement

Xiangyang Shen: Conceptualization, Methodology, Resources, Visualization, Writing – original draft, Writing – review & editing. Feng Liu: Formal analysis, Methodology, Supervision. Jinyuan Guan: Data curation, Investigation, Validation. Fuyu Dong: Formal analysis, Funding acquisition, Project administration, Writing – review & editing. Yue Zhang: Data curation, Funding acquisition, Supervision. Zihe Guo: Investigation, Validation. Ye Yuan: Formal analysis, Resources. Binbin Wang: Conceptualization, Software. Liangshun Luo: Investigation, Methodology. Yanqing Su: Conceptualization, Formal analysis. Jun Cheng: Conceptualization, Validation. Xiaoguang Yuan: Formal analysis, Methodology. Peter K. Liaw: Funding acquisition.

### Declaration of competing interest

We declare that we have no financial and personal relationships with other people or organizations that can inappropriately influence our work, there is no professional or other personal interest of any nature or kind in any product, service and/or company that could be construed as influencing the position presented in, or the review of, the manuscript entitled "Effect of hydrogen on thermal deformation behavior and microstructure evolution of MoNbHfZrTi refractory high-entropy alloy".

## Data availability

The authors do not have permission to share data.

### Acknowledgments

The present work was supported by the National Natural Science Foundation of China (52101037, 52271249), the Grant Plan for Young and Middle-aged Innovation Scientists of Shenyang Government (RC210058), Basic Scientific Research Project of Education Department of Liaoning Province (LJKMZ20220466), Natural Science Foundation of Liaoning Province, and project supported by State Key Laboratory of Powder Metallurgy, Central South University, Changsha, China. P. K.

Liaw very much appreciates the support from (1) the National Science Foundation (DMR-1611180, 1809640, and 2226508) and (2) the US Army Research Office (W911NF-13–1-0438 and W911NF-19–2-0049).

#### References

- [1] J.-W. Yeh, S.-K. Chen, S.-J. Lin, J.-Y. Gan, T.-S. Chin, T.-T. Shun, C.-H. Tsau, S.-Y. Chang, Nanostructured high-entropy alloys with multiple principal elements: novel alloy design concepts and outcomes, Adv. Eng. Mater. 6 (2004) 299–303.
- [2] B. Cantor, I.T.H. Chang, P. Knight, A.J.B. Vincent, Microstructural development in equiatomic multicomponent alloys, Mater. Sci. Eng. A 375–377 (2004) 213–218.
- [3] D.B. Miracle, O.N. Senkov, A critical review of high entropy alloys and related concepts, Acta Mater. 122 (2017) 448–511.
- [4] Y. Zhang, T.T. Zuo, Z. Tang, M.C. Gao, K.A. Dahmen, P.K. Liaw, Z.P. Lu, Microstructures and properties of high-entropy alloys, Prog. Mater. Sci. 61 (2014) 1–93
- [5] L. Qiao, A. Bao, Z. Lai, Y. Liu, J. Zhu, Y. Wang, Alloy design and properties optimization of multi-component alloy based on solidification characteristics, Mater. Sci. Eng. A 805 (2021) 140576.
- [6] J. Dabrowa, M. Zajusz, W. Kucza, G. Cieślak, K. Berent, T. Czeppe, T. Kulik, M. Danielewski, Demystifying the sluggish diffusion effect in high entropy alloys, J. Alloys Compd. 783 (2019) 193–207.
- [7] F. Maresca, W.A. Curtin, Theory of screw dislocation strengthening in random BCC alloys from dilute to "High-Entropy" alloys, Acta Mater. 182 (2020) 144–162.
- [8] B.X. Cao, C. Wang, T. Yang, C.T. Liu, Cocktail effects in understanding the stability and properties of face-centered-cubic high-entropy alloys at ambient and cryogenic temperatures, Scripta Mater. 187 (2020) 250–255.
- [9] X. Ren, Y. Li, Y. Qi, B. Wang, Review on preparation technology and properties of refractory high entropy alloys, Materials 15 (2022) 2931.
- [10] O.N. Senkov, D.B. Miracle, K.J. Chaput, J.-P. Couzinie, Development and exploration of refractory high entropy alloys—a review, J. Mater. Res. 33 (2018) 3092–3128.
- [11] A. Shafiee, J. Moon, H.S. Kim, M. Jahazi, M. Nili-Ahmadabadi, Precipitation behaviour and mechanical properties of a new wrought high entropy superalloy, Mater. Sci. Eng. A 749 (2019) 271–280.
- [12] Y. Wu, J. Si, D. Lin, T. Wang, W.Y. Wang, Y. Wang, Z. Liu, X. Hui, Phase stability and mechanical properties of AlHfNbTiZr high-entropy alloys, Mater. Sci. Eng. A 724 (2018) 249–259.
- [13] T.M. Butler, K.J. Chaput, Native oxidation resistance of Al20Nb30Ta10Ti30Zr10 refractory complex concentrated alloy (RCCA), J. Alloys Compd. 787 (2019) 606–617.
- [14] X. Xie, N. Li, W. Liu, S. Huang, X. He, Q. Yu, H. Xiong, E. Wang, X. Hou, Research progress of refractory high entropy alloys: a review, Chin. J. Mech. Eng. 35 (2022) 142.
- [15] S. Alvi, F. Akhtar, High temperature tribology of CuMoTaWV high entropy alloy, Wear 426–427 (2019) 412–419.
- [16] Z. Guo, X. Shen, F. Liu, J. Guan, Y. Zhang, F. Dong, Y. Wang, X. Yuan, B. Wang, L. Luo, Y. Su, J. Cheng, Microstructure and mechanical properties of Alx (TiZrTa0.7NbMo) refractory high-entropy alloys, J. Alloys Compd. 960 (2023) 170739.
- [17] R. John, M.K. Dash, B.S. Murty, D. Fabijanic, Effect of temperature and strain rate on the deformation behaviour and microstructure of Al0.7CoCrFeNi high entropy alloy, Mater. Sci. Eng. A 856 (2022) 143933.
- [18] Z. Savaedi, R. Motallebi, H. Mirzadeh, A review of hot deformation behavior and constitutive models to predict flow stress of high-entropy alloys, J. Alloys Compd. 903 (2022) 163964.
- [19] W.-H. Liao, C.-W. Tsai, Y.-C. Tseng, W.-R. Wang, C.-S. Chen, J.-W. Yeh, Exploring hot deformation behavior of equimolar CoCrFeNi high-entropy alloy through constitutive equations and microstructure characterization, Mater. Char. (2023) 11224
- [20] W.H. Johnson, On some remarkable changes produced in iron and steel by the action of hydrogen and acids, Nature 11 (1875) 393, 393.
- [21] J. Lee, H. Park, M. Kim, H.-J. Kim, J. Suh, N. Kang, Role of hydrogen and temperature in hydrogen embrittlement of equimolar CoCrFeMnNi high-entropy alloy, Met. Mater. Int. 27 (2021) 166–174.
- [22] S. Zhang, M. Liu, Y. Luo, L. Wang, Z. Wang, Z. Wang, F. Li, Q. Shen, X. Wang, Immunity of Al0.25CoCrFeNi high-entropy alloy to hydrogen embrittlement, Mater. Sci. Eng. A 821 (2021) 141590.
- [23] K. Ichii, M. Koyama, C.C. Tasan, K. Tsuzaki, Comparative study of hydrogen embrittlement in stable and metastable high-entropy alloys, Scripta Mater. 150 (2018) 74–77.
- [24] J. Hu, J. Zhang, H. Xiao, L. Xie, G. Sun, H. Shen, P. Li, J. Zhang, X. Zu, The effect of hydrogen on the mechanical properties of high entropy alloy TiZrHfMoNb: firstprinciples investigation, J. Alloys Compd. 879 (2021) 160482.
- [25] X.L. Ren, P.H. Shi, W.W. Zhang, X.Y. Wu, Q. Xu, Y.X. Wang, Swamps of hydrogen in equiatomic FeCuCrMnMo alloys: first-principles calculations, Acta Mater. 180 (2019) 189–198.
- [26] J. Yi, X. Zhuang, J. He, M. He, W. Liu, S. Wang, Effect of Mo doping on the gaseous hydrogen embrittlement of a CoCrNi medium-entropy alloy, Corrosion Sci. 189 (2021) 109628.
- [27] Q. Li, J.W. Mo, S.H. Ma, F.H. Duan, Y.L. Zhao, S.F. Liu, W.H. Liu, S.J. Zhao, C. T. Liu, P.K. Liaw, T. Yang, Defeating hydrogen-induced grain-boundary embrittlement via triggering unusual interfacial segregation in FeCrCoNi-type high-entropy alloys, Acta Mater. 241 (2022) 118410.

- [28] Y. Zhao, D.-H. Lee, M.-Y. Seok, J.-A. Lee, M.P. Phaniraj, J.-Y. Suh, H.-Y. Ha, J.-Y. Kim, U. Ramamurty, J. Jang, Resistance of CoCrFeMnNi high-entropy alloy to gaseous hydrogen embrittlement, Scripta Mater. 135 (2017) 54–58.
- [29] Zwicker U, Schleicher HW, Process for Improving the Workability of Titanium Alloys, (n.d.).
- [30] O.N. Senkov, J.J. Jonas, F.H. Froes, Recent advances in the thermohydrogen processing of titanium alloys, JOM 48 (1996) 42–47.
- [31] J.I. Qazi, O.N. Senkov, J. Rahim, F.H. (Sam) Froes, Kinetics of martensite decomposition in Ti-6Al-4V-xH alloys, Mater. Sci. Eng. A 359 (2003) 137–149.
- [32] Y.Q. Su, S.J. Wang, L.S. Luo, L. Wang, F.Y. Dong, J.J. Guo, H.Z. Fu, Gradient microstructure of TC21 alloy induced by hydrogen during hydrogenation, Int. J. Hydrogen Energy 37 (2012) 19210–19218.
- [33] Y. Zong, D. Shan, Y. Lu, B. Guo, Effect of 0.3wt%H addition on the high temperature deformation behaviors of Ti-6Al-4V alloy, Int. J. Hydrogen Energy 32 (2007) 3936–3940.
- [34] A. Nicolaÿ, G. Fiorucci, J.M. Franchet, J. Cormier, N. Bozzolo, Influence of strain rate on subsolvus dynamic and post-dynamic recrystallization kinetics of Inconel 718, Acta Mater. 174 (2019) 406–417.
- [35] G. He, Y. Zhao, B. Gan, X. Sheng, Y. Liu, L. Tan, Mechanism of grain refinement in an equiatomic medium-entropy alloy CrCoNi during hot deformation, J. Alloys Compd. 815 (2020) 152382
- [36] H.T. Jeong, H.K. Park, W.J. Kim, Dynamic recrystallization and hot deformation mechanisms of a eutectic Al0.7CoCrFeMnNi high-entropy alloy, J. Alloys Compd. 871 (2021) 159488.
- [37] Q. Liu, G. Wang, Y. Liu, X. Sui, Y. Chen, S. Luo, Hot deformation behaviors of an ultrafine-grained MoNbTaTiV refractory high-entropy alloy fabricated by powder metallurgy, Mater. Sci. Eng. A 809 (2021) 140922.
- [38] N. Prasad, N. Bibhanshu, N. Nayan, G.S. Avadhani, S. Suwas, Hot deformation behavior of the high-entropy alloy CoCuFeMnNi, J. Mater. Res. 34 (2019)
- [39] R.R. Eleti, A.H. Chokshi, A. Shibata, N. Tsuji, Unique high-temperature deformation dominated by grain boundary sliding in heterogeneous necklace structure formed by dynamic recrystallization in HfNbTaTiZr BCC refractory high entropy alloy, Acta Mater. 183 (2020) 64–77.
- [40] P. Rodriguez, Serrated plastic flow, Bull. Mater. Sci. 6 (1984) 653-663.
- [41] Y. Zhang, J.P. Liu, S.Y. Chen, X. Xie, P.K. Liaw, K.A. Dahmen, J.W. Qiao, Y. L. Wang, Serration and noise behaviors in materials, Prog. Mater. Sci. 90 (2017) 358–460.
- [42] J.W. Qiao, Y. Zhang, P.K. Liaw, Serrated flow kinetics in a Zr-based bulk metallic glass, Intermetallics 18 (2010) 2057–2064.
- [43] B. Wang, X. Shan, H. Zhao, S. Bai, B. Wang, Y. Tian, Y. Tang, High-temperature deformation behavior and microstructural evolution of NbZrTiTa refractory high entropy alloy, J. Alloys Compd. 936 (2023) 168059.
- [44] F. Dong, Y. Yuan, W. Li, Y. Zhang, P.K. Liaw, X. Yuan, H. Huang, Hot deformation behavior and processing maps of an equiatomic MoNbHfZrTi refractory high entropy alloy, Intermetallics 126 (2020) 106921.

- [45] M.B. Djukic, G.M. Bakic, V. Sijacki Zeravcic, A. Sedmak, B. Rajicic, The synergistic action and interplay of hydrogen embrittlement mechanisms in steels and iron: localized plasticity and decohesion, Eng. Fract. Mech. 216 (2019) 106528.
- [46] T. Li, Y. Lu, Z. Li, T. Wang, T. Li, Hot deformation behavior and microstructure evolution of non-equimolar Ti2ZrHfV0.5Ta0.2 refractory high-entropy alloy, Intermetallics 146 (2022) 107586.
- [47] L. Liu, Q. Ding, Y. Zhong, J. Zou, J. Wu, Y.-L. Chiu, J. Li, Z. Zhang, Q. Yu, Z. Shen, Dislocation network in additive manufactured steel breaks strength–ductility tradeoff, Mater. Today 21 (2018) 354–361.
- [48] D.R. Trinkle, C. Woodward, The chemistry of deformation: how solutes soften pure metals, Science 310 (2005) 1665–1667.
- [49] C. Lee, F. Maresca, R. Feng, Y. Chou, T. Ungar, M. Widom, K. An, J.D. Poplawsky, Y.-C. Chou, P.K. Liaw, W.A. Curtin, Strength can be controlled by edge dislocations in refractory high-entropy alloys, Nat. Commun. 12 (2021) 5474.
- [50] K.-K. Tseng, H.-H. Huang, W.-R. Wang, J.-W. Yeh, C.-W. Tsai, Edge-dislocation-induced ultrahigh elevated-temperature strength of HfMoNbTaW refractory high-entropy alloys, Sci. Technol. Adv. Mater. 23 (2022) 642–654.
- [51] Q. Zhao, H. Luo, Z. Yang, Z. Pan, Z. Wang, R.K. Islamgaliev, X. Li, Hydrogen induced cracking behavior of the dual-phase Co30Cr10Fe10Al18Ni30Mo2 eutectic high entropy alloy, Int. J. Hydrogen Energy 50 (2024) 134–147.
- [52] R.D. Doherty, D.A. Hughes, F.J. Humphreys, J.J. Jonas, D.J. Jensen, M.E. Kassner, W.E. King, T.R. McNelley, H.J. McQueen, A.D. Rollett, Current issues in recrystallization: a review, Mater. Sci. Eng. A 238 (1997) 219–274.
- [53] S. Vervynckt, K. Verbeken, P. Thibaux, Y. Houbaert, Recrystallization-precipitation interaction during austenite hot deformation of a Nb microalloyed steel, Mater. Sci. Eng. A 528 (2011) 5519–5528.
- [54] G.S. Rohrer, Introduction to grains, phases, and interfaces—an interpretation of microstructure, Trans. AIME 175 (1948) 15–51. C.S. Smith, Metall. Mater. Trans. A. 41 (2010) 1063–1100.
- [55] F.J. Humphreys, The nucleation of recrystallization at second phase particles in deformed aluminium, Acta Metall. 25 (1977) 1323–1344.
- [56] J. Konrad, S. Zaefferer, D. Raabe, Investigation of orientation gradients around a hard Laves particle in a warm-rolled Fe3Al-based alloy using a 3D EBSD-FIB technique, Acta Mater. 54 (2006) 1369–1380.
- [57] W. Xu, M. Ferry, J. Cairney, F. Humphreys, Three-dimensional investigation of particle-stimulated nucleation in a nickel alloy, Acta Mater. 55 (2007) 5157–5167.
- [58] K. Huang, R.E. Logé, A review of dynamic recrystallization phenomena in metallic materials, Mater. Des. 111 (2016) 548–574.
- [59] X. Yang, Z. Yan, P. Dong, B. Cheng, J. Zhang, T. Zhang, H. Zhang, W. Wang, Surface modification of aluminum alloy by incorporation of AlCoCrFeNi high entropy alloy particles via underwater friction stir processing, Surf. Coat. Technol. 385 (2020) 125438.
- [60] X. Yang, P. Dong, Z. Yan, B. Cheng, X. Zhai, H. Chen, H. Zhang, W. Wang, AlCoCrFeNi high-entropy alloy particle reinforced 5083Al matrix composites with fine grain structure fabricated by submerged friction stir processing, J. Alloys Compd. 836 (2020) 155411.